Article

The Role of Phase Separation on Rayleigh-Plateau Type Instabilities in Alloys

Ryan H. Allaire, Lou Kondic, Linda J. Cummings, Philip D. Rack,* and Miguel Fuentes-Cabrera*

Cite This: *J. Phys. Chem. C* 2021, 125, 5723−5731

Read Online

ACCESS | Metrics & More | Article Recommendations | SI Supporting Information

ABSTRACT: Classical molecular dynamics (MD) simulations are used to investigate the role of phase separation (PS) on the Rayleigh-Plateau (RP) instability. Ni−Ag bulk structures are created at temperatures (2000 K and 1400 K) that generate different PS length scales, λ_{PS}, relative to the RP instability length scale, λ_{RP}. Rectanguloids are then cut from the bulk structures and patterned with a perturbation of certain amplitude and wavelength, λ_{RP}. It is found that when $\lambda_{PS} \ll \lambda_{RP}$ (2000 K), the patterned rectanguloids break up into nanoparticles in a manner consistent with classical RP theory, whereas when $\lambda_{PS} \ll \lambda_{RP}$ (1400 K), soluto-capillarity affects the RP instability significantly. Specifically, since Ag has a lower surface energy than Ni, Ag migrates to cover neighboring Ni regions, therefore modifying the RP instability. Thus, we demonstrate that the phase separation length scale of an immiscible alloy can be exploited to direct the assembly of functional bimetallic alloys.
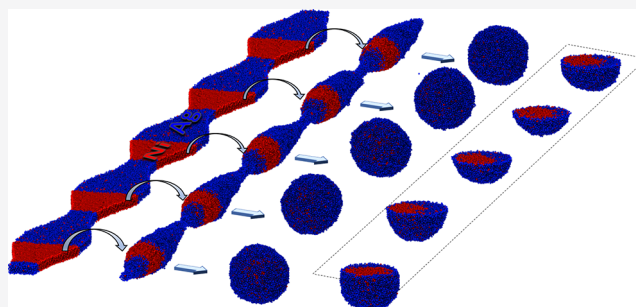
1. INTRODUCTION

This work extends recent studies that explore how hydrodynamic instabilities in two-dimensional single-component thin metal films[1−3] and nanostructures[4,5] can be used to create different arrays of organized and correlated nanoparticles. The Rayleigh-Plateau (RP) instability, for instance, is a phenomenon that emerges in a liquid jet: as different modes of surface-tension-driven instabilities evolve on the surface of the liquid, the fastest-growing mode dominates and pinches the liquid jet at regular points along its length, breaking it into droplets. The spinodal and nucleation types of instability for a thin film deposited on a substrate are other examples; in such a configuration, thin films break up and may generate nanoparticles with a correlated size and length scale; see recent reviews[6,7] for more details. Other effects can compete with (or enhance) these types of instabilities. For example, thermal gradients can lead to gradients in surface energy (the thermocapillary effect, also known as thermal Marangoni effect) which may influence the dewetting mechanism.[8,9] Similarly, differences in chemical concentration may lead to gradients in surface energy,[10] known as the soluto-capillary effect (or concentration Marangoni effect). In this work, we focus on how RP hydrodynamic instabilities compete with soluto-capillarity. We leverage so-called synthetic perturbations, which are lithographically patterned rectanguloids with varicose edge perturbations, to control the competition/cooperation of the RP and soluto-capillarity. Synthetic perturbations in elemental liquid metals have been demonstrated experimentally and verified via detailed simulations to direct the precise assembly of nanoparticle arrays via unstable RP instabilities.[11,12]

We use here classical molecular dynamics (MD) simulations to study the Ni−Ag system at $Ni_{0.5}Ag_{0.5}$ chemical composition and focus on the influence of phase separation (PS) on RP-type hydrodynamic instabilities. Several previous MD studies have investigated the spinodal[13,14] and RP[13,15,16] instabilities as well as other dewetting phenomena[17−25] in single-component films. Additionally, several groups have studied liquid-state PS in metallic systems such as Al−Pb[26] and Al−Ge−Mn;[27] see also our recent work exploring the role that a liquid-vacuum and liquid-substrate interface has on the phase separation in Ag−Ni single drops.[28] The Ag−Ni system is interesting in that Ag is an efficient plasmonic material and Ni is ferromagnetic, thus in principle, bifunctional magnetoplasmonic nanoparticles can be generated.[29] Recent experimental pulsed laser-induced dewetting studies of various alloys for plasmonic,[30−34] magnetic,[35] and magnetoplasmonic[36−38] systems have been performed. For instance, control of the thin film thickness of gold and silver affects the resultant nanoparticle size distribution, which subsequently affects the surface plasmon resonance energy.
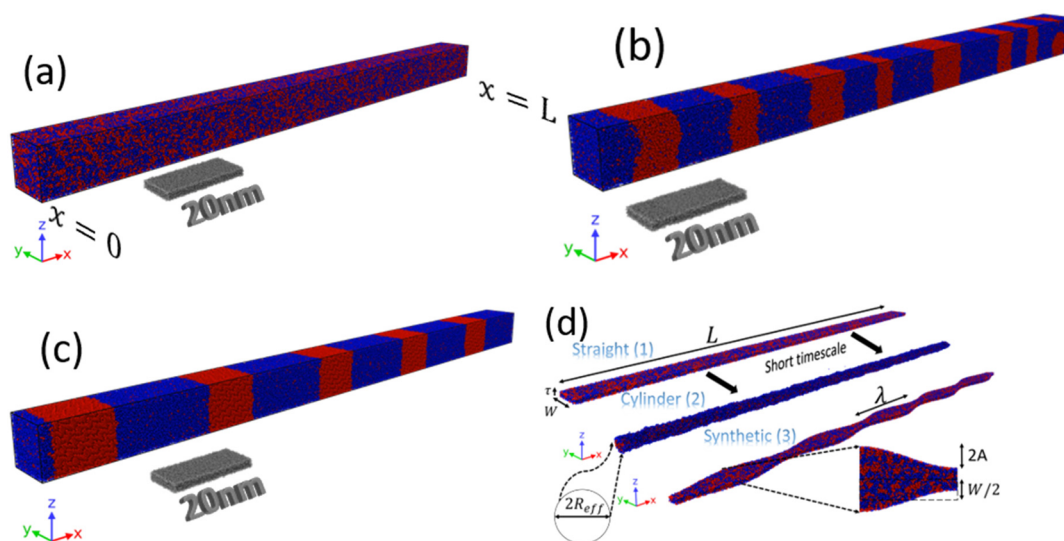
Figure 1. Equilibrated $Ni_{0.5}Ag_{0.5}$ bulk structures at (a) 2000 K and (b, c) 1400 K. In part a, phase separation leads to the formation of small clusters of Ni and Ag, whereas in part b, PS results in the formation of unequally sized stripes along the x-axis. In part c, PS stripes were created to have a fixed length (the difference in size is due to the unequal atomic volumes of the two phases). (d) Straight lines (1) and lines with perturbations (referred to as synthetic lines) (3) are cut from bulks (parts a–c) (here, the lines from part a are shown). In vacuum, the lines quickly deform into cylinders (2). The cross sections of 1 and 3 are both rectangles of thickness, τ but 1 has a fixed width, W, whereas the width in 3 varies with x. The cross sections of 2 are circles of radius R_{eff}. For 3, the perturbations have wavelength λ and amplitude A (half the distance of peak to trough). Color code: Ni (red), Ag (blue).

2. MATERIALS AND METHODS

Bulk structures of $Ni_{0.5}Ag_{0.5}$ were equilibrated at 3000 K using a small initial sample of 256 atoms with the isothermal–isobaric (NPT), canonical (NVT), and microcanonical (NVE) ensembles, respectively. We employed both the Nose-Hoover thermostat and barostat[39] with a temperature damping parameter of 100 fs and pressure damping parameter of 0.5 fs. The embedded-atom method (EAM) potential derived by Zhou et al.[40] was used to describe the Ni–Ni, Ag–Ag, and Ni–Ag interactions (see our previous work for details[28]). Subsequently, the small samples were expanded to a large bulk of 829440 atoms and equilibrated (using the same ensembles) from 3000 to 1400 K in 200 K increments, similar to our previous work.[28] For temperatures between 1800 and 3000 K, the bulk structure was sequentially equilibrated using 400 ps of NPT, 600 ps of NVT, and 200 ps of NVE (total of 1.2 ns). Thus, the cooling rate from 3000 to 1800 K was 1.67×10^{11} K/s. At 1600 K, the bulk is equilibrated for 4.8 ns (400 ps NPT, 2400 ps NVT, 2000 ps NVE) so the cooling rate from 1800 to 1600 K was 0.42×10^{11} K/s. We cooled the bulk to 1400 K from 1600 K in 6.6 ns (400 ps NPT, 1800 ps NVT, and 4400 ps NVE), so the cooling rate was 0.30×10^{11} K/s. Note that lower temperatures required more time to equilibrate temperature and energy.

In our previous work, we found that phase separation of Ni and Ag phases in a $Ni_{0.5}Ag_{0.5}$ bulk started at temperatures below 2400 K, consistent with the equilibrium phase diagram, and that larger phase separation length scales emerged as the temperature was lowered.[28] When the bulk $Ni_{0.5}Ag_{0.5}$ was suspended in vacuum, such that a free surface existed, a Ag@Ni core–shell morphology emerged due to Ag's lower surface energy. On the basis of our previous work, here, we consider temperature as a proxy to control the PS length scale, which we call λ_{PS}. We focus on two temperatures: 2000 K, which is in the immiscible Ag–Ni liquid–liquid phase region of the phase diagram, and 1400 K, which for a bulk material is in the Ag–Ni

liquid–solid phase. In materials at the nanoscale, however, it is well-known that the melting point is suppressed. Recently, Ridings et al.[41] showed that for the effective radii investigated below (~18 Å), the (100) and (110) planes have surface melting temperatures ~1300 and 1200 K, respectively. Furthermore, the "bulk" cylinder core has a melting temperature close to 1400 K. Thus, in the dewetting studies below, the suppressed nickel melting point leads to a Ag–Ni (liquid–liquid) system where some nanogranular solid Ni could exist in the cylinder core. It should be noted, however, that the RP-like instabilities, while derived for liquid filaments, are operative in both solid[42,43] and granular materials.[44,45]

To emulate pulsed laser-induced dewetting experiments, where metal nano structures are lithographically patterned onto substrates, we cut thin rectanguloids (referred to as lines for simplicity) from the bulk structures with lengthwise (x) perturbations of a prescribed wavelength and amplitude. We denote the length of the respective bulk and associated line by L and impose periodic boundary conditions at $x = 0, L$. Figure 1 shows bulk structures created at 2000 K, part a; and at 1400 K, part b. Note that both the lengths of the bulks in Figure 1a,b and the width of the respective lines are not constructed exactly equal (see the Supporting Information, Section S.1, for more details).

As seen in Figure 1a, at 2000 K, small clusters of Ni and Ag are formed. Using the cluster analysis tool in Ovito,[46] the average sizes of Ni and Ag clusters (assuming clusters are all densely[47] filled spheres) are found to be 6.2 and 6.7 Å respectively, and $\lambda_{PS} = 12.9$ Å is defined to be the sum of the Ni and Ag average cluster sizes.

In Figure 1b, at 1400 K, Ni (red) and Ag (blue) stripes form along the longitudinal axis, x. There is some variation in the lengths of each of the stripes as the line was equilibrated from high temperature. The PS length scale is defined as a sum of the average lengths of both Ni and Ag stripes, $\lambda_{PS} = 170.7$ Å.

To emphasize and better interrogate the competing effects that phase separation has on the dewetting dynamics, we equilibrated so-called "forced" periodic structures with regions of equal number of Ag and Ni regions at length scales similar to those observed in Figure 1b. The bulk (Figure 1b) was first created with 5120 atoms: equal parts of Ni and Ag. The energy was minimized, and both NPT/NVT ensembles were used to equilibrate pressure, volume, and temperature at 300 K, 1000 K, and then finally 1400 K. The small bulk structure was then replicated (expanded) into one containing 921600 atoms (this is where the stripe patterns emerge) and subsequently equilibrated with 1.2 ns of NVT and 9 ns of NVE, which we found to be sufficient for convergence. Note that controlled bimetal patterns can be achieved via lithography[10] (albeit at larger length scales) and chemical synthesis routes.[48]

Similar to Figure 1b, Ni and Ag stripes are formed, but now, by design, each Ag−Ni stripe pair has a fixed length; note also that each Ag and Ni stripe has approximately the same number of atoms, but the atoms are closer to each other for Ni (the atomic volume for Ag is roughly 1.66 times larger than that for Ni at 1400 K). The PS length scale, defined in the same manner as in Figure 1b, is λ_{PS} = 315.6 Å.

Figure 1d shows an example of lines cut from the bulk structure at 2000 K (Figure 1a). Here, image (1) shows a straight line of length L and width W, and image (3) is a line of the same length L with applied perturbations of amplitude A and wavelength λ (referred to as a synthetic line). Note that, when suspended in vacuum, both straight and synthetic lines quickly form a cylinder, so as to minimize surface energy (such a cylinder is shown in Figure 1d, image (2)); even in the case of the synthetic lines, cylinders form faster than line breakup, as discussed below.

2.1. Rayleigh-Plateau Theory for Liquid Metals. Consider a perturbed liquid cylinder of radius $R(x,t)$ with axis, x and surface given by

$$R(x, t) = R_0 + A\exp(ikx + \omega t) \tag{1}$$

where R_0 is the average radius and A, k, ω are the perturbation amplitude, wavenumber, and growth rate, respectively, with $A \ll R_0$. Classical RP theory predicts that such small perturbations to liquid cylinders in vacuum, neglecting viscosity, will grow at the rate given by

$$\omega^2 = \frac{\gamma}{\rho R_0^3} kR_0 \frac{I_1(kR_0)}{I_0(kR_0)}(1 - k^2 R_0^2) \tag{2}$$

where γ and ρ are the liquid surface tension and density, and I_0, I_1 are Bessel functions of the first kind of the zeroth and first order, respectively. In this paper, we focus on the (unstable) modes that grow ($\omega > 0$, only possible when $kR_0 < 1$). Of the unstable modes, the one that grows the fastest is the one with wavenumber k_m, found by maximizing $\omega(k)$ in eq 2 with given values of γ, ρ (see Table 1), and R_0 (see Table 2), given by

$$k_m R_0 \approx 0.697. \tag{3}$$

The corresponding wavelength, $\lambda_m = 2\pi/k_m$, of this mode depends only on the initial radius of the cylinder and is given by $\lambda_m = 9.01\, R_0$.

Previously, we have shown that synthetic perturbations characterized by an unstable RP wavelength can be used to control the breakup of nanoscale metallic liquid lines into droplets of desired size and spacing.[11,12] Here, we investigate whether the RP instability can be used to describe the breakup

Table 1. Material Parameters for Ni, Ag, and Ni$_{0.5}$Ag$_{0.5}$ Alloy at Both 2000 K and 1400 K Obtained by Linearly Extrapolating Properties from the Melting Temperature[a]

	ρ_{2000K} (kg/m^3)	γ_{2000K} (N/m)	ρ_{1400K} (kg/m^3)	γ_{1400K} (N/m)
Ni	7587.2	1.7	8283.2	1.9
Ag	8652.4	0.8	9196.4	0.9
Ni$_{0.5}$Ag$_{0.5}$	8119.8	1.2	8739.8	1.4

[a]Properties for the alloy are found by averaging.

of Ni$_{0.5}$Ag$_{0.5}$ lines (rather than pure element cylinders) in vacuum. Although the RP theory technically only applies to single-element liquids, we apply it to the Ni$_{0.5}$Ag$_{0.5}$ alloy by averaging densities and surface liquid tensions for the single elements (Vegard's law) as given in Table 1. As mentioned earlier, when suspended in vacuum, the lines transform into cylinders of effective radius R_{eff} perturbed along the long axis with effective amplitude A_{eff} (in the case of straight lines, A_{eff} = 0). For simplicity, we define the effective radius to be the radius of the cylinder that results from the straight lines, found by equating cross-sectional areas, and is given by

$$R_{eff} = \sqrt{\frac{W\tau}{\pi}}$$

where τ is the line thickness, which we fix in all cases as $\tau = \frac{W}{5}$. For the synthetic perturbation cases, the effective amplitude can be found by equating the cross-sectional area of the perturbation troughs to that of the thinnest part of the perturbed cylinder. Since the width of the line at troughs is $(W - 2A)$ and the radius of the thinnest parts of the cylinder is $R_{eff} - A_{eff}$, equating cross-sectional areas, $(W - 2A)\tau = \pi (R_{eff} - A_{eff})^2$, we find the effective amplitude

$$A_{eff} = \sqrt{\frac{W\tau}{\pi}} - \sqrt{\frac{(W - 2A)\tau}{\pi}}$$

For each part of Figure 1a−c, the wavelength is chosen so that $L = 5\lambda$, where L is the (fixed) length of the respective bulk. With the values of the widths W given in Table 2, the chosen wavelengths correspond to unstable perturbations (stability curves will be shown shortly). By removing atoms from the bulk structures, Ni$_{0.5}$Ag$_{0.5}$ lines of certain width, wavelength, amplitude, and thickness (values are given in Table 2) are extracted at 2000 K and 1400 K. We use **A**, **B**, and **C** to denote the straight and synthetic lines cut from parts a−c of Figure 1, respectively.

Figure 2 displays the theoretical dispersion curves for the material parameters given in Table 1 using $R_0 = R_{eff}$ in eq 2 for **A**, **B**, and **C**. The values of the chosen wavelengths for **A**, **B**, and **C** are given by vertical dashed lines and are denoted here by λ_A, λ_B, and λ_C, respectively. Except for the differences in maximum growth rate, ω_m at $\lambda_m = 9.01 R_{eff}$, these curves are very similar. Note that we have used a nonmaximum wavelength, $\lambda > \lambda_m$, in each case so that the RP dynamics occur on a longer time scale (see the Supporting Information, Figure.S.1, for a case where λ_m is used). The numerical values of λ and $\omega(\lambda)$ are given in Table 2 along with the widths, effective radii, lengths, temperatures, and PS length scales. The values of A_{eff} will be discussed further at the end of the Results section. The question now is how do the values for ω and λ obtained from the RP analysis differ from those obtained via MD simulations? Specifically, we are interested in studying

Table 2. Temperature; Width W; Wavelength λ; Phase Separation Length Scale λ_{PS}; and Length L, for Lines A, B, and C; Transformed Cylinder Effective Radius R_{eff}; Associated RP Growth-Rate Prediction ω, via eq 2

Line	Temp (K)	W (Å)	R_{eff} (Å)	λ (Å)	λ_{PS} (Å)	L (Å)	ω (1/ps)
A	2000	65.0	16.4	292.6	13.0	1463.2	4.3×10^{-2}
B	1400	63.6	16.1	286.7	170.7	1433.7	4.5×10^{-2}
C	1400	71.0	17.9	319.8	315.6	1598.9	3.8×10^{-2}
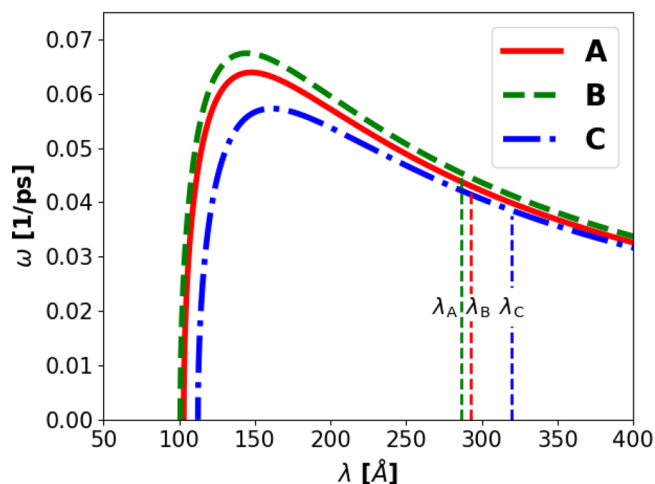
Figure 2. RP dispersion curves, using Eq. 2 with effective cylinder radius R_{eff}, where the growth rate is calculated using the geometric parameters from lines **A** (red solid line), **B** (green dashed line), and **C** (blue dot-dashed line) (Table 2), and the material parameters given in Table 1. The vertical dashed lines correspond to the wavelengths used in the corresponding simulations.

how phase separation interacts with the RP instability and affects the breakup of the lines.

3. RESULTS

Below, we show how temperature and the phase separation length scale affect the breakup of straight and synthetic lines into nanoparticles, producing results that differ from those predicted by the RP theory. Unless otherwise stated, we set the

RP length scales to the wavelengths provided in Table 2 and denote them as λ_{RP} to differentiate from λ_{PS}.

Figure 3 shows the temporal evolution of Ni$_{0.5}$Ag$_{0.5}$ lines in vacuum. Note that the lines are evolved using the NVE ensemble. Straight and synthetic lines are shown in the left and right columns of Figure 3, respectively. Labels (i–v) indicate the time stamps at which the lines undergo significant changes during the simulation: (i) indicates the initial configuration; (ii) the time at which surface perturbations develop; (iii) the time immediately prior to the breakup of the line; (iv) the intermediate time between the breakup and the formation of nanoparticles; and (v) the time of nanoparticle formation. On panel b, the wavelength of the imposed perturbation is also indicated. In Figure 3, a key difference between the initial structures (row (i)) is in the relative sizes of the PS and RP length scales. At 2000 K, the PS length scale is a stable RP wavelength (surface perturbations due to PS would decay: $\omega(\lambda_{PS}) < 0$ in Figure 2), whereas at 1400 K, surface perturbations of wavelength λ_{PS} are RP-unstable ($\omega(\lambda_{RP}) > 0$). In the following text, we refer to a small PS length scale as one where PS-induced perturbations decay and a large PS length scale as one where they grow.

At 2000 K, the PS length scale is small and the straight line (Figure 3a) develops surface perturbations at 11 ps (row (ii)) due to small fluctuations in the initial configuration rather than perturbations induced by PS. By comparison, in the synthetic lines (Figure 3b), at 10 ps (row (ii)), the perturbation is already well developed as expected, since the perturbation of wavelength λ_{RP} was already prescribed in the initial configuration. Nanoparticles are formed in the synthetic lines 90 ps faster than in the straight lines. Five nanoparticles are
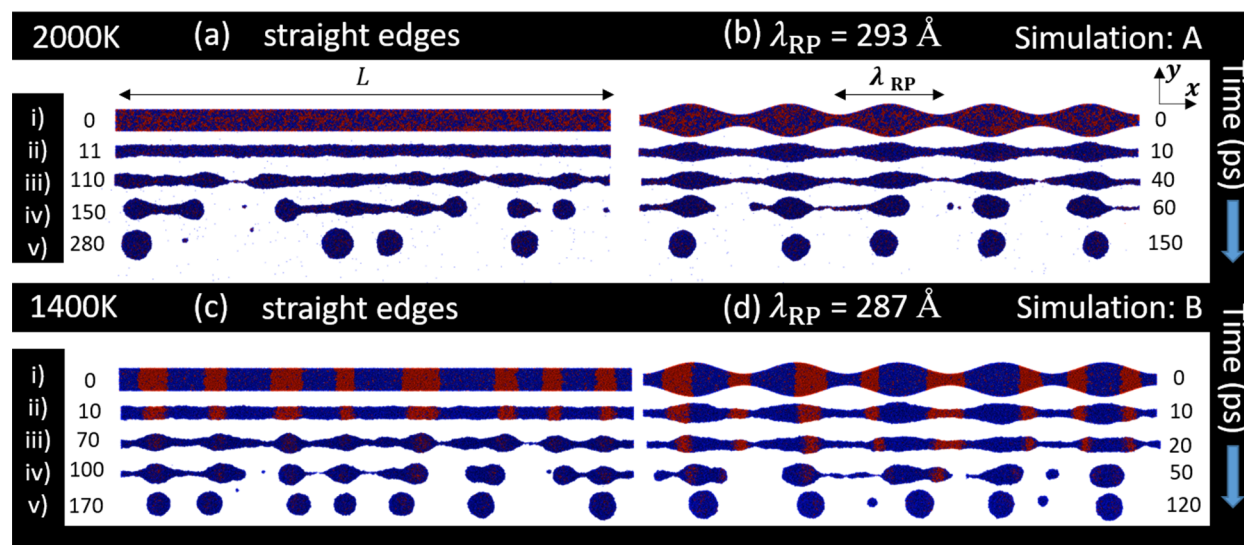
Figure 3. Time evolution of straight (left) and synthetic (right) lines at 2000 K (a, b) and 1400 K (c, d). The parameters for 2000 K and 1400 K are given in Table 2 under **A** and **B**, respectively. Time labels in ps (see text below) are placed next to the corresponding lines. Color code: Ni (red), Ag (blue).
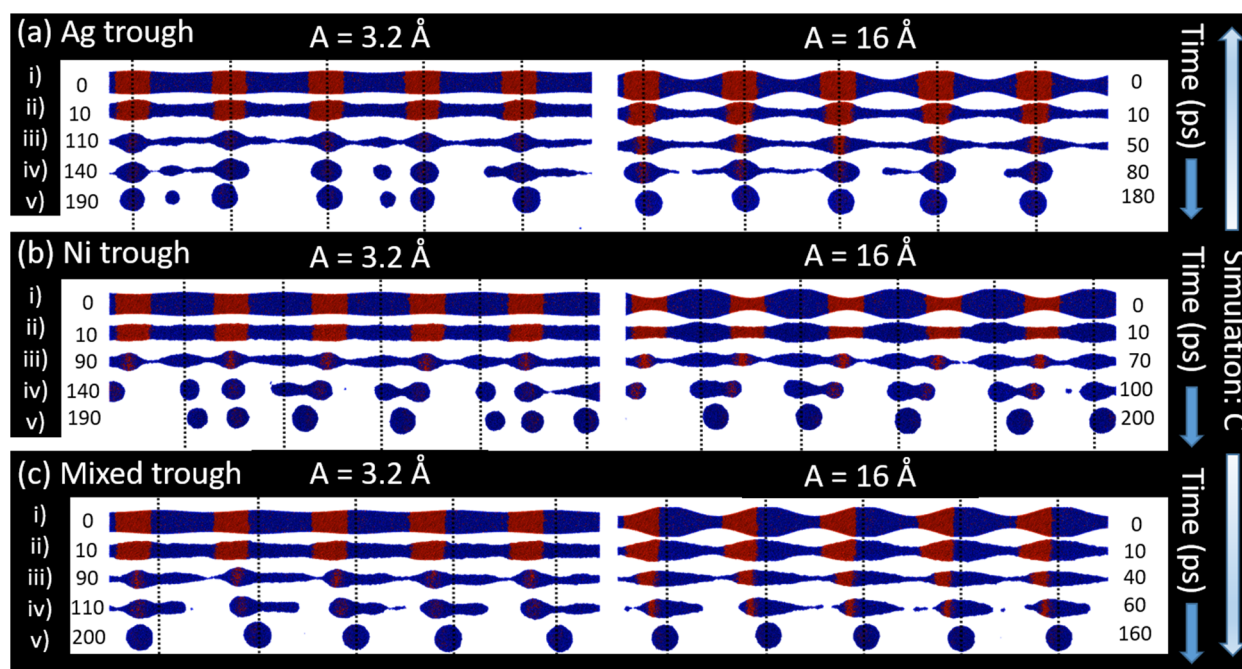
Figure 4. Time evolution of synthetic lines for Ag-rich troughs (a), Ni-rich troughs (b), and mixed Ni and Ag troughs (c) for perturbations of amplitudes A = 3.2 Å (left) and A = 16.0 Å (right). The labels i–v correspond to different time intervals in ps with description as in Figure 3. Guides (dotted lines) are placed at the location of the original synthetic peak position in (i). The geometric details for the lines are given in Table 2 under simulation **C**. Color code: Ni (red), Ag (blue).

formed in the synthetic lines, which corresponds well to the five patterned wavelengths, whereas in the straight lines the asymmetry of line breakup results in shortening of the resulting line parts via material transport, leading to (in this case) four nanoparticles only. For instance, note that, following line breakup the central part of Figure 3a, row (iv) at 150 ps has 3 varicose perturbations (and thus one would expect 4 droplets), but the breakup only occurs near the middle of this region (the surrounding instabilities are suppressed) resulting in just two particles. The two droplets in the rightmost region of Figure 3a, row (iv), on the other hand, coalesce into one droplet by row (v). The locations of the nanoparticles differ in the straight and synthetic lines. For the latter, as expected, nanoparticles form at the peaks of the perturbation and are well spaced; for the straight lines, the nanoparticles are not equidistant/periodic. For both types of lines, the resultant nanoparticles are homogeneous and contain Ni and Ag in a liquid-like configuration with a small phase separation length scale.

At 1400 K (Figure 3c,d), the PS length scale is large. As the simulations proceed, the troughs of the perturbation develop primarily in Ag-rich regions or at the interface between adjacent Ag-rich/Ni-rich regions. Both lines break up faster than their 2000 K counterparts, 110 and 30 ps faster for the straight and synthetic lines, respectively. This is somewhat counterintuitive: 1400 K is below the melting point of Ni (1728 K) and less than 200 K above the melting point of Ag (1235K). Therefore, at 1400 K, one would expect the atom mobility to be less than at 2000 K and thus breakup to take longer. The reason behind a faster breakup at 1400 K is due to the thinning of the line in Ag-rich locations (Ag "migrates" to neighboring regions faster than does Ni due to the lower melting temperature). The straight line, for instance, forms seven nanoparticles, whereas the synthetic line forms five. Interestingly, these nanoparticles are not uniform but have a core–shell like structure, with Ag in the shell and Ni in the

core (see particle slices in Supporting Information; Section S.3).

For reference, pure Ni and Ag straight lines with comparable R_{eff} = 16.1 Å were simulated at 1400 K (and equilibrated similar to the alloys as described above). The evolution of the pure metals (see Supporting Information; Section S.4) confirms that the dewetting instability is RP-like even in the Ni metal. In fact, the initial breakup time for Ni (~120 ps) is faster than that for Ag (140 ps), which confirms that the Ni is largely, if not fully, liquefied, as a solid phase filament would dewet much more slowly, even if still RP-like. The faster Ni dewetting time is consistent with Ni having a higher surface energy than Ag. Finally, we also compared the radial distribution functions for Ni–Ni in the bulk and in the filament at 1400 K (from Figure 1b and 3c(ii), respectively; see Supporting Information, Section S.4). As expected, the peak in the Ni–Ni radial distribution function for the ~16 Å cylinder is smaller than the bulk, suggestive of a reduced order and at least partial melting.

From the results above, it appears that at 1400 K for lines where the PS length scale is on the order of the RP instability length scale, the soluto-capillary Ag migration induces unstable perturbations that modify the existing RP instability and affect breakup. To investigate this effect more carefully, we created synthetic lines and prescribed perturbations (cut from bulk Figure 1c) where troughs are located in the Ag-rich or Ni-rich regions, or close to the interface between these two regions; see Figure 4a–c, respectively. In all these lines, the lengths of Ni and neighboring Ag regions sum to the RP wavelength, λ_{RP}. As stated earlier, the length of the Ag phase-separated regions (average length of blue regions in Figure 3c) is slightly larger than that of the Ni regions. This difference is small, however, thus the structures seen for the lines in Figure 4 correspond to the regime where the PS length scales of Ni and Ag are approximately half the RP length scale. Two different

perturbation amplitudes were considered, 3.2 and 16 Å, which we refer to as small and large amplitudes.

Figure 4 shows the temporal evolution of $Ni_{0.5}Ag_{0.5}$ lines at 1400 K. The troughs of the perturbations are either located at (a) Ag-rich regions (referred to as Ag trough), (b) Ni-rich regions (Ni trough), or (c) mixed Ni/Ag regions (Mixed trough). The main finding is that the location of the resultant nanoparticles differs between (a), (b), and (c).

The primary difference between the small (Figure 4, left column) and large amplitude (Figure 4, right column) is the time it takes the lines to reach the first pinch. In general, the large amplitude lines pinch faster than their small amplitude counterparts since there is less material in the trough of the perturbation. The large amplitude case can be thought of as further along in the destabilization process that is inherited from the RP instability. The largest difference in the pinch time (60 ps) occurs in case (a). Further, the small amplitude case generates small secondary or satellite particles near two of the perturbation peak regions in Figure 4b, left column.

Figure 4a−c collectively highlights the importance of the initial trough composition. Consider, in the large amplitude cases (right panel of Figure 4), the position of the resultant nanoparticles in (v) relative to the trough guides (the dashed vertical lines). In part a, the nanoparticles are primarily located at the peak of the perturbation (the dashed lines), which is consistent with the typical RP instability where the material thins at the troughs and accumulates at the peaks. In comparison, the resultant nanoparticles in part b are slightly misaligned relative to the prescribed peaks. This difference can be explained as follows. The RP instability tends to thin and pinch the lines at the trough of the perturbation. If the trough is Ag-rich, the Ag migration and the RP instability cooperate in breaking the line. However, if the trough is Ni-rich, Ag migration and the RP instability compete. Cooperation and competition should be more apparent in the small amplitude case, since in this case breakup occurs later. Indeed, the left panel of Figure 4 shows that for the Ag-rich trough, part a, the primary particle positions are aligned with the peak regions. For the Ni-rich trough, part b, the trough coarsens slightly as the Ag soluto-capillary effect opposes the RP instability. The initially Ag-rich regions eventually act as the pinch points and the primary particles end slightly off-center from the original synthetic perturbation peak; secondary particles also emerge due to the inter-Ag filament thinning. Notably, all secondary satellite particles are nearly pure Ag and thus, while most of the core−shell nanoparticles are $\sim Ni_{0.5}Ag_{0.5}$, primary particles that neighbor a secondary satellite are Ag-deficient.

To test the competition between the soluto-capillary effect and the RP, we use the PS length scale, λ_{PS} from Figure 4 (see C from Table 2 for the parameters); in addition, we pattern the synthetic perturbations at longer (slower growth rate) unstable wavelengths (λ_{RP} = 533.0 Å; see Figure 2, simulation C) and variable amplitudes. Figure 5 illustrates the time evolution of these structures with the following initial amplitudes in (i): a, 3.2 Å; b, 5 Å; and c, 6 Å (larger amplitudes were also simulated, and the outcomes are similar to part c). The times (i−iv) are similar to those described for Figure 3 and Figure 4. Time (v) represents the earliest time stamp of full droplet coalescence. The main finding is that the number of resultant primary droplets depends on the amplitude of the prescribed perturbation. At low amplitude ($A < 5$ Å; part a), the soluto-capillary driven instability clearly dominates as 5 primary nanoparticles (droplets roughly comparable in size) result and
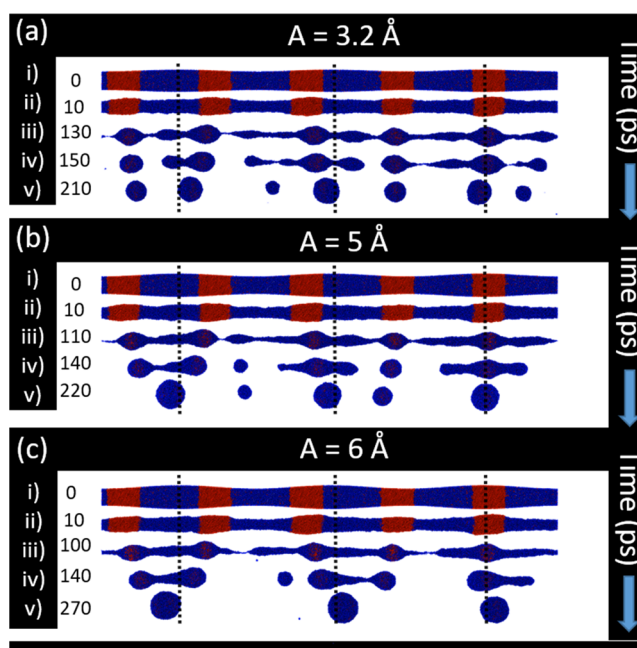
Figure 5. Time evolution of synthetic lines patterned with wavelength λ_{RP} = 533.0 Å and amplitudes A = 3.2 Å (a), A = 5 Å (b), and A = 6 Å (c). Time labels (in ps) are placed next to the corresponding lines. The labels (i−v) correspond to those in Figure 4. Guides (dotted lines) are placed at the location of the original peak in (i). Except for the wavelength, the geometric details for the lines are as given in Table 2 under simulation **C**. Color code: Ni (red), Ag (blue).

are positioned near the original Ni-rich regions (the Ag migration offsets the resultant droplet positioning slightly and leads to formation of 2 smaller satellite droplets). At intermediate amplitudes (5 Å $< A < 6$ Å; part b), there is a transition: 4 primary nanoparticles result (also one satellite droplet), and the coalescence of two Ni regions occurs adjacent to the peak located in the Ag region (left-most droplet). Finally, at higher amplitudes ($A > 6$ Å; part c), the RP driven instability dominates as 3 primary nanoparticles result and are located at the peaks of the synthetic perturbations.

Finally, we compare MD pinch times of the nanoscale alloys to RP theory pinch times. Table 3 lists the MD simulated breakup times for the simulations reported here (where data was recorded every 10 ps) and the prediction made via RP theory. The theoretical breakup times are based on the linear growth rate ω, amplitude, A, and effective radius, R_{eff}, via

$$t_{pinch} = \frac{-\ln\left(\frac{A_{eff}}{R_{eff}}\right)}{\omega} \tag{4}$$

Though detailed statistics and higher time resolution output would enhance the accuracy of the MD pinch time, the simulated breakup times agree well with the theoretical predictions even though, in some instances, PS competes with or enhances the RP instability. Thus, it appears that the soluto-capillary dynamics occur on time scales similar[1] to those of traditional RP.

4. CONCLUSIONS

Molecular dynamics (MD) simulations are used to investigate the effect of phase separation on the breakup mechanism of thin liquid lines of $Ni_{0.5}Ag_{0.5}$ alloy in a vacuum. At 2000 K, the

Table 3. Comparison of Simulated Breakup (Pinch) Times and Predicted Pinch Times According to RP Theory for the Simulations A, B, and C as Well as Others Not Described in the Text

Temp (K)	Reference	Amplitude (Å)	Eff. Amplitude (Å)	MD Pinch Time (ps)	RP Theory Pinch Time (ps)
2000	Figure 3 (2000 K)	16	4.7	40	29
1400	Figure 3 (1400 K)	16	4.7	30	27
1400	Figure 4 (Ni Trough)	3.2	0.8	100	80
1400	Figure 4 (Ni Trough)	16	4.6	70	35
1400	Figure 4 (Ag Trough)	3.2	0.8	120	80
1400	Figure 4 (Ag Trough)	16	4.6	60	35
1400	Figure 4 (Mixed Trough)	3.2	0.8	100	80
1400	Figure 4 (Mixed Trough)	16	4.6	50	35

NiAg structures are mostly homogeneous and the defining phase separation (PS) length scale, λ_{PS}, is much smaller than the Rayleigh-Plateau (RP) length scale, λ_{RP}. Here, breakup occurs in the classical manner, as if the structure were homogeneous with material parameters averaged over those of the constituents, and resultant nanoparticles are aligned with the peak of the underlying synthetic perturbations. At 1400 K, the PS length scale is comparable to the RP length scale and the long axis migration of Ag onto Ni influences the resultant droplet location relative to the initial perturbation. The positioning of the final droplets is found to be influenced by the composition of the trough of the undulations and the strength of the RP instability (controlled by the amplitude). For small amplitudes, PS competes with RP when lines contain Ni-rich troughs, resulting in some primary nanoparticles of Ag@Ni core−shell morphology aligned with the initially Ni-rich regions as well as some pure Ag satellite drops. When the troughs contain either Ag-rich or mixed NiAg troughs, the RP instability is complemented by the PS structure resulting in primary nanoparticles aligned with the peaks of the initial perturbation. In general, these resultant nanoparticles are of Ag@Ni core−shell morphology, but for the low amplitude, Ag-rich trough, some pure Ag satellite droplets are formed.

The soluto-capillary/RP competition is further interrogated by the simulation of lines with PS length scales shorter than λ_{RP}, so that growth of the RP instability is slow relative to PS-induced perturbations. We demonstrate that the tuning of the synthetic perturbation amplitude dictates whether soluto-capillarity or RP drives the instability. With the average line radius of 35.5 Å kept in mind, when the amplitude is sufficiently small (here, $A < 5$ Å), soluto-capillarity dominates. Increasing the amplitude increases the "strength" of the RP instability, and for $A > 6$ Å, the RP mechanism dominates. The MD breakup times of the nanoscale alloys are found to be in good agreement with the predictions of RP theory.

ASSOCIATED CONTENT

Supporting Information

The Supporting Information is available free of charge at https://pubs.acs.org/doi/10.1021/acs.jpcc.0c08720.

Section S.1: discussion of the construction and equilibration of the bulk structures. Section S.2: time evolution of lines at maximum RP wavelength. Section S.3: details of the creation of the lines and slices of the final nanoparticles. Section S.4: Simulations of pure metals at 1400 K and Ni−Ni radial distribution functions of NiAg bulk and cylinder at 1400 K (PDF)

AUTHOR INFORMATION

Corresponding Authors

Miguel Fuentes-Cabrera − *Center for Nanophase Materials Sciences, Oak Ridge National Laboratory, Oak Ridge, Tennessee 37831, United States;* orcid.org/0000-0001-7912-7079; Email: fuentescabma@ornl.gov

Philip D. Rack − *Center for Nanophase Materials Sciences, Oak Ridge National Laboratory, Oak Ridge, Tennessee 37831, United States; Department of Materials Science and Engineering, The University of Tennessee, Knoxville, Tennessee 37996, United States;* orcid.org/0000-0002-9964-3254; Email: prack@utk.edu

Authors

Ryan H. Allaire − *Department of Mathematical Sciences, New Jersey Institute of Technology, Newark, New Jersey 07102, United States*

Lou Kondic − *Department of Mathematical Sciences, New Jersey Institute of Technology, Newark, New Jersey 07102, United States;* orcid.org/0000-0001-6966-9851

Linda J. Cummings − *Department of Mathematical Sciences, New Jersey Institute of Technology, Newark, New Jersey 07102, United States*

Complete contact information is available at:
https://pubs.acs.org/10.1021/acs.jpcc.0c08720

Notes

The authors declare no competing financial interest.

ADDITIONAL NOTE

[1] Although the MD pinch times are comparable in size to the RP predictions, they are consistently longer, possibly due to nonlinear effects which slow down the exponential growth predicted by linear stability analysis.

■ REFERENCES

(1) Bischof, J.; Scherer, D.; Herminghaus, S.; Leiderer, P. Dewetting Modes of Thin Metallic Films: Nucleation of Holes and Spinodal Dewetting. *Phys. Rev. Lett.* **1996**, 77 (8), 1536−1539.

(2) Favazza, C.; Kalyanaraman, R.; Sureshkumar, R. Robust nanopatterning by laser-induced dewetting of metal nanofilms. *Nanotechnology* **2006**, 17 (16), 4229−4234.

(3) Favazza, C.; Trice, J.; Krishna, H.; Kalyanaraman, R.; Sureshkumar, R. Laser-induced short- and long-range orderings of Co nanoparticles on SiO2. *Appl. Phys. Lett.* **2006**, 88 (15), 153118.

(4) Kondic, L.; Diez, J. A.; Rack, P. D.; Guan, Y.; Fowlkes, J. D. Nanoparticle assembly via the dewetting of patterned thin metal lines: Understanding the instability mechanisms. *Phys. Rev. E* **2009**, 79 (2), 026302.

(5) Wu, Y.; Fowlkes, J. D.; Rack, P. D.; Diez, J. A.; Kondic, L. On the Breakup of Patterned Nanoscale Copper Rings into Droplets via Pulsed-Laser-Induced Dewetting: Competing Liquid-Phase Instability and Transport Mechanisms. *Langmuir* **2010**, 26 (14), 11972−11979.

(6) Kondic, L.; González, A. G.; Diez, J. A.; Fowlkes, J. D.; Rack, P. Liquid-State Dewetting of Pulsed-Laser-Heated Nanoscale Metal Films and Other Geometries. *Annu. Rev. Fluid Mech.* **2020**, 52 (1), 235−262.

(7) Ruffino, F.; Grimaldi, M. G., Nanostructuration of Thin Metal Films by Pulsed Laser Irradiations: A Review. *Nanomaterials* **2019**, 9 (8).

(8) Atena, A.; Khenner, M. Thermocapillary effects in driven dewetting and self assembly of pulsed-laser-irradiated metallic films. *Phys. Rev. B: Condens. Matter Mater. Phys.* **2009**, 80 (7), 075402.

(9) Trice, J.; Favazza, C.; Thomas, D.; Garcia, H.; Kalyanaraman, R.; Sureshkumar, R. Novel Self-Organization Mechanism in Ultrathin Liquid Films: Theory and Experiment. *Phys. Rev. Lett.* **2008**, 101 (1), 017802.

(10) Hartnett, C. A.; Seric, I.; Mahady, K.; Kondic, L.; Afkhami, S.; Fowlkes, J. D.; Rack, P. D. Exploiting the Marangoni Effect To Initiate Instabilities and Direct the Assembly of Liquid Metal Filaments. *Langmuir* **2017**, 33 (33), 8123−8128.

(11) Fowlkes, J. D.; Kondic, L.; Diez, J.; Wu, Y.; Rack, P. D. Self-Assembly versus Directed Assembly of Nanoparticles via Pulsed Laser Induced Dewetting of Patterned Metal Films. *Nano Lett.* **2011**, 11 (6), 2478−2485.

(12) Fowlkes, J. D.; Roberts, N. A.; Wu, Y.; Diez, J. A.; González, A. G.; Hartnett, C.; Mahady, K.; Afkhami, S.; Kondic, L.; Rack, P. D. Hierarchical Nanoparticle Ensembles Synthesized by Liquid Phase Directed Self-Assembly. *Nano Lett.* **2014**, 14 (2), 774−782.

(13) Nguyen, T. D.; Fuentes-Cabrera, M.; Fowlkes, J. D.; Diez, J. A.; González, A. G.; Kondic, L.; Rack, P. D. Competition between Collapse and Breakup in Nanometer-Sized Thin Rings Using Molecular Dynamics and Continuum Modeling. *Langmuir* **2012**, 28 (39), 13960−13967.

(14) Nguyen, T. D.; Fuentes-Cabrera, M.; Fowlkes, J. D.; Rack, P. D. Coexistence of spinodal instability and thermal nucleation in thin-film rupture: Insights from molecular levels. *Phys. Rev. E* **2014**, 89 (3), 032403.

(15) Fowlkes, J.; Horton, S.; Fuentes-Cabrera, M.; Rack, P. D. Signatures of the Rayleigh-Plateau Instability Revealed by Imposing Synthetic Perturbations on Nanometer-Sized Liquid Metals on Substrates. *Angew. Chem., Int. Ed.* **2012**, 51 (35), 8768−8772.

(16) Kawano, S. Molecular dynamics of rupture phenomena in a liquid thread. *Phys. Rev. E: Stat. Phys., Plasmas, Fluids, Relat. Interdiscip. Top.* **1998**, 58 (4), 4468−4472.

(17) Akbarzadeh, H.; Yaghoubi, H. Molecular dynamics simulations of silver nanocluster supported on carbon nanotube. *J. Colloid Interface Sci.* **2014**, 418, 178−184.

(18) Bertrand, E.; Blake, T. D.; De Coninck, J. Dynamics of dewetting at the nanoscale. *Eur. Phys. J.: Spec. Top.* **2009**, 166 (1), 173−176.

(19) Bertrand, E.; Blake, T. D.; Ledauphin, V.; Ogonowski, G.; De Coninck, J.; Fornasiero, D.; Ralston, J. Dynamics of Dewetting at the Nanoscale Using Molecular Dynamics. *Langmuir* **2007**, 23 (7), 3774−3785.

(20) Blake, T. D.; Clarke, A.; De Coninck, J.; de Ruijter, M. J. Contact Angle Relaxation during Droplet Spreading: Comparison between Molecular Kinetic Theory and Molecular Dynamics. *Langmuir* **1997**, 13 (7), 2164−2166.

(21) De Coninck, J.; Blake, T. D. Wetting and Molecular Dynamics Simulations of Simple Liquids. *Annu. Rev. Mater. Res.* **2008**, 38 (1), 1−22.

(22) de Ruijter, M. J.; Blake, T. D.; De Coninck, J. Dynamic Wetting Studied by Molecular Modeling Simulations of Droplet Spreading. *Langmuir* **1999**, 15 (22), 7836−7847.

(23) Fuentes-Cabrera, M.; Rhodes, B. H.; Baskes, M. I.; Terrones, H.; Fowlkes, J. D.; Simpson, M. L.; Rack, P. D. Controlling the Velocity of Jumping Nanodroplets Via Their Initial Shape and Temperature. *ACS Nano* **2011**, 5 (9), 7130−7136.

(24) Fuentes-Cabrera, M.; Rhodes, B. H.; Fowlkes, J. D.; López-Benzanilla, A.; Terrones, H.; Simpson, M. L.; Rack, P. D. Molecular dynamics study of the dewetting of copper on graphite and graphene: Implications for nanoscale self-assembly. *Phys. Rev. E* **2011**, 83 (4), 041603.

(25) Kumar, S. Spreading and orientation of silver nano-drops over a flat graphene substrate: An atomistic investigation. *Carbon* **2018**, 138, 26−41.

(26) Li, T.; Wang, Z.; Duan, Y.; Li, J.; Li, H. Molecular dynamics study on the formation of self-organized core/shell structures in the Pb alloy at the nanoscale. *RSC Adv.* **2017**, 7 (84), 53509−53515.

(27) Tang, Y.; Wang, X. D.; Cao, Q. P.; Liu, S. Y.; Zhang, D. X.; Zhang, J.; Wu, Z. H.; Hu, T. D.; Xie, H. L.; Xiao, T. Q.; Jiang, J. Z. Nanometer-scale phase separation in Al60Ge30Mn10 amorphous alloy. *J. Alloys Compd.* **2019**, 802, 166−172.

(28) Allaire, R. H.; Dhakane, A.; Emery, R.; Ganesh, P.; Rack, P. D.; Kondic, L.; Cummings, L.; Fuentes-Cabrera, M., Surface, Interface, and Temperature Effects on the Phase Separation and Nanoparticle Self Assembly of Bi-Metallic Ni0.5Ag0.5: A Molecular Dynamics Study. *Nanomaterials* **2019**, 9 (7).

(29) Garfinkel, D. A.; Pakeltis, G.; Tang, N.; Ivanov, I. N.; Fowlkes, J. D.; Gilbert, D. A.; Rack, P. D., Optical and Magnetic Properties of Ag-Ni Bimetallic Nanoparticles Assembled via Pulsed Laser-Induced Dewetting. *ACS Omega* **2020**.519285

(30) Beliatis, M. J.; Henley, S. J.; Silva, S. R. P. Engineering the plasmon resonance of large area bimetallic nanoparticle films by laser nanostructuring for chemical sensors. *Opt. Lett.* **2011**, 36 (8), 1362−1364.

(31) Censabella, M.; Ruffino, F.; Zimbone, M.; Bruno, E.; Grimaldi, M. G. Self-Organization Based Fabrication of Bimetallic PtPd Nanoparticles on Transparent Conductive Oxide Substrates. *Phys. Status Solidi A* **2018**, 215 (3), 1700524.

(32) Oh, Y.; Lee, J.; Lee, M. Fabrication of Ag-Au bimetallic nanoparticles by laser-induced dewetting of bilayer films. *Appl. Surf. Sci.* **2018**, 434, 1293−1299.

(33) Wu, Y.; Fowlkes, J. D.; Rack, P. D. The optical properties of Cu-Ni nanoparticles produced via pulsed laser dewetting of ultrathin films: The effect of nanoparticle size and composition on the plasmon response. *J. Mater. Res.* **2011**, 26 (2), 277−287.

(34) Wu, Y.; Li, G.; Cherqui, C.; Bigelow, N. W.; Thakkar, N.; Masiello, D. J.; Camden, J. P.; Rack, P. D. Electron Energy Loss Spectroscopy Study of the Full Plasmonic Spectrum of Self-Assembled Au-Ag Alloy Nanoparticles: Unraveling Size, Composition, and Substrate Effects. *ACS Photonics* **2016**, 3 (1), 130−138.

(35) Krishna, H.; Gangopadhyay, A. K.; Strader, J.; Kalyanaraman, R. Nanosecond laser-induced synthesis of nanoparticles with tailorable magneticanisotropy. *J. Magn. Magn. Mater.* **2011**, 323 (3), 356−362.

(36) McKeown, J. T.; Wu, Y.; Fowlkes, J. D.; Rack, P. D.; Campbell, G. H. Simultaneous In-Situ Synthesis and Characterization of Co@Cu Core-Shell Nanoparticle Arrays. *Adv. Mater.* **2015**, 27 (6), 1060−1065.

(37) Sachan, R.; Yadavali, S.; Shirato, N.; Krishna, H.; Ramos, V.; Duscher, G.; Pennycook, S. J.; Gangopadhyay, A. K.; Garcia, H.; Kalyanaraman, R. Self-organized bimetallic Ag-Co nanoparticles with tunable localized surface plasmons showing high environmental stability and sensitivity. *Nanotechnology* **2012**, *23* (27), 275604.

(38) Sosunov, A. V.; Spivak, L. V. Magnetic properties of bimetallic Au/Co nanoparticles prepared by thermal laser treatment. *Phys. Solid State* **2016**, *58* (7), 1371−1374.

(39) Frenkel, D.; Smit, B., Chapter 6 - Molecular Dynamics in Various Ensembles. In *Understanding Molecular Simulation* (Second ed.), Frenkel, D.; Smit, B., Eds. Academic Press: San Diego, 2002; pp 139−163.

(40) Zhou, X. W.; Johnson, R. A.; Wadley, H. N. G. Misfit-energy-increasing dislocations in vapor-deposited CoFe/NiFe multilayers. *Phys. Rev. B: Condens. Matter Mater. Phys.* **2004**, *69* (14), 144113.

(41) Ridings, K. M.; Aldershof, T. S.; Hendy, S. C. Surface melting and breakup of metal nanowires: Theory and molecular dynamics simulation. *J. Chem. Phys.* **2019**, *150* (9), 094705.

(42) Jeong, J.; Choi, K.; Ye, J. Investigation of a Rayleigh-Like Instability During the Solid-State Dewetting of Single-Crystal Nickel and Palladium Films. *J. Korean Phys. Soc.* **2018**, *73* (1), 90−94.

(43) Thompson, C. V. Solid-State Dewetting of Thin Films. *Annu. Rev. Mater. Res.* **2012**, *42* (1), 399−434.

(44) Prado, G.; Amarouchene, Y.; Kellay, H. Experimental Evidence of a Rayleigh-Plateau Instability in Free Falling Granular Jets. *Phys. Rev. Lett.* **2011**, *106* (19), 198001.

(45) Ulrich, S.; Zippelius, A. Stability of Freely Falling Granular Streams. *Phys. Rev. Lett.* **2012**, *109* (16), 166001.

(46) Stukowski, A. Visualization and analysis of atomistic simulation data with OVITO-the Open Visualization Tool. *Modell. Simul. Mater. Sci. Eng.* **2010**, *18* (1), 015012.

(47) Berryman, J. G. Random close packing of hard spheres and disks. *Phys. Rev. A: At., Mol, Opt. Phys.* **1983**, *27* (2), 1053−1061.

(48) Mayer, M.; Scarabelli, L.; March, K.; Altantzis, T.; Tebbe, M.; Kociak, M.; Bals, S.; García de Abajo, F. J.; Fery, A.; Liz-Marzán, L. M. Controlled Living Nanowire Growth: Precise Control over the Morphology and Optical Properties of AgAuAg Bimetallic Nanowires. *Nano Lett.* **2015**, *15* (8), 5427−5437.